Polydopamine-coated downconversion nanoparticle as an efficient dual-modal near-infrared-II fluorescence and photoacoustic contrast agent for non-invasive visualization of gastrointestinal tract *in vivo*

Lina Ma[a,b], Sa Huang[c,**], Shuqing He[b], Zhenxin Wang[a,***], Zhen Cheng[b,*]

[a]State Key Laboratory of Electroanalytical Chemistry, Changchun Institute of Applied Chemistry, Chinese Academy of Sciences, Changchun, 130022, PR China

[b]Molecular Imaging Program at Stanford (MIPS), Bio-X Program, Department of Radiology, Stanford University, Stanford, CA, 94305-5344, United States

[c]Department of Radiology, The Second Hospital of Jilin University, Changchun, 130041, PR China

Abstract

Herein, a multifunctional dual-modal imaging probe is successfully developed to integrate the advantages of second near-infrared window (NIR-II, 1000–1700 nm) fluorescence imaging (FI) and photoacoustic imaging (PAI) with the ultimate goal of improving diseases diagnosis and management. Melanin-inspired polydopamine (PDA) polymer coated $NaYF_4:Yb^{3+},Er^{3+}@NaYbF_4@NaYF_4:Nd^{3+}$ down conversion nanoparticles (DCNPs) is designed *via* water-in-oil microemulsion method, which comprises a DCNP core, acting as the NIR-II optical imaging agent, and a PDA shell, acting as the PA contrast agent. By taking the advantages of high spatial resolution and excellent temporal resolution, the dual-modal contrast agent is capable for high sensitivity real-time visualization of gastrointestinal tract, diagnosis of gastrointestinal peristalsis disorder and NIR-II FI-guided intestinal obstruction surgery. All of the above results demonstrate the great potential of DCNP@PDA NP as an efficient NIR-II/PAI dual-modal contrast agent for precision medicine.

Keywords

Near-infrared window II fluorescence imaging; Photoacoustic imaging; Down conversion nanoparticles; Visualization of gastrointestinal tract; Image-guided surgery

1. Introduction

Molecular imaging plays a significant role in organism structure research, cancer diagnosis, intraoperative guidance and post-surgery evaluation (Ai et al., 2018; Choi et al., 2017; Kim et al., 2018). A rapid progress of the single-mode imaging has appeared in particular for decades due to their improved clinical curative effect and the lower medical costs for patients (Keereweer et al., 2013; Nguyen and Tsien, 2013; Vahrmeijer et al., 2013). Multimodality molecular imaging is one of the most valuable innovations as a medical imaging tool, which can not only circumvent the weaknesses of single modality but also integrate all the advantages of two or more imaging modalities (Kircher et al., 2012). Consequently, various multimodal approaches have been explored in order to improve the diagnostic accuracy. Besides, new multimodal imaging technologies can effectively relieve discomfort feeling by reducing the scanning or operation time and may reduce time cost by simplifying workflows (Cheng et al., 2017; Dai et al., 2017; Qin et al., 2013).

Fluorescence imaging (FI) is currently highly interactive for *in vivo* observing and assessing biological processes because of its fast feedback, high sensitivity, high spatiotemporal resolution, nonionizing radiation, ease of use and low cost, *etc.*(Shou et al., 2017). Furthermore, FI has gained significant attentions in current image-guided surgery practice especially when coupled with FDA-approved near infrared (NIR) probes, such as indocyanine green (ICG) and Methylene blue (MB), which can be targeted to help remove diseased tissue and retain healthy tissue through specific visualization (Hong et al., 2017; Gibbs, 2012). Despite many advantages, the low tissue penetration depth and signal-to-noise ratio of FI seriously limit its further applications (Fan and Zhang, 2019). A promising approach to overcome these problems is to make bioimaging in the second NIR window (NIR-II, 1000–1700 nm) compared with the photo-emission window of FI in visible (400–700 nm) and first NIR window (NIR-I, 700–900 nm). NIR-II FI has much deeper tissue penetration and higher spatiotemporal resolution due to low photon absorption and scattering and low auto-fluorescence of normal biological tissues (Liu et al., 2018). Although the FI has high spatial resolution, the tissue penetration of FI is still limited by optical attenuation. Photoacoustic imaging (PAI) is a relatively new biomedical imaging modality based on the photoacoustic effect, which can extend the limitation of imaging depth to a few centimeters and generate high-resolution optical images (Wang and Hu, 2012). To date, PAI shows considerable potential in many critical clinical fields, such as early diagnosis of prostate and breast cancer, detection of tumor metastases, endoscopic gastrointestinal (GI) imaging and treatment monitoring (Jiang and Pu, 2017). Recently, the fusion of NIR-II FI and PAI technologies have been used for biomedical applications (Zhang et al., 2019; Guo et al., 2019; Hu et al., 2019; Wang et al., 2019; He et al., 2019; Sheng et al., 2018; Yang et al., 2017; Cheng et al., 2017), which enables people to 'See' and 'Listen' the interactions between light and biological tissues and molecular probes. These new techniques may provide promising approaches to improve optical imaging of diseases.

There are some emerging materials as candidates of NIR-II FI, such as quantum dots (QDs) (Hong et al., 2012; Zhang et al. 2012, 2018), single-walled carbon nanotubes (SWNTs) (Antaris et al., 2013; Wong et al., 2017; Yi et al., 2012), organic dye molecules (Antaris et al. 2016, 2017; Li et al., 2018), and conjugated polymers (Hong et al., 2014). It remains a

key challenge to explore NIR-II emissive fluorophores in order to obtain new NIR-II FI with desirable properties. Lanthanide doped down-conversion nanoparticles (DCNPs) take the advantages of low photobleaching, long luminescence lifetimes, low long-term cytotoxicity and narrow emission band widths, processing a widely applied prospect in bioimaging applications (Fan et al., 2018; Xu et al., 2019; Zhong et al., 2017). In particular, Nd^{3+}-doped DCNPs have attracted considerable attention since Nd^{3+} ion is not only able to emit NIR-II emission (~1050 and ~1300 nm) (Chen et al., 2012) but also efficiently sensitize Yb^{3+} ions under excited at a biocompatible wavelength of ~800 nm where absorption by water is minimal (Xie et al., 2013).

In this study, bright NIR-II emissive DCNPs ($NaYF_4:Yb^{3+},Er^{3+}@NaYbF_4@NaYF_4:Nd^{3+}$ core@shell@shell structure, CSS) were synthesized according to the literature method (Shao et al., 2016). Hexagonal $NaYF_4$ with low phonon energy is chosen as the inorganic host material to build the CSS structure (Chen et al., 2014). The existence of the $NaYbF_4$ layer in the CSS structure is important to maximize emission from the emitter, as this layer can suppress detrimental cross-relaxation processes between Er^{3+} and Nd^{3+} by spatial isolation, and enhance energy transfer from the outer shell to the core by introducing Yb-mediated energy migration. Under excited by 808 nm, the energy hops in a certain sequence of Nd^{3+} ions (outermost layer),Yb^{3+} ions (secondary outer layer) and Yb^{3+}/Er^{3+} ion pair (core), and then the CSS structure DCNPs emit narrow large Stoke-shifted emission in the NIR-II range. The CSS structure plays double roles here, suppressing surface-related quenching of the core nanocrystal by spatial isolation from the environment, and eliciting directional energy flow all the way to the core nanocrystal. The melanin-inspired polydopamine (PDA) polymer coated DCNPs (DCNP@PDA NPs) were obtained through reactions of oleic acid-capped DCNPs with dopamine *via* our previously reported water-in-oil microemulsion method (Liu et al., 2015; Ma et al., 2017). PDA, a synthetic melanin, as a new kind of versatile biomolecules, formed by the simple oxidative self-polymerization of dopamine, has attracted extensively attention in many fields, especially in the biomedical field due to its intrinsic high biocompatibility (Lee et al., 2007; Liu et al. 2013, 2014). PDA contains abundant catechol that can react with thiol- and amino-terminated molecules via Michael addition and Schiff base reactions. Therefore, PDA can be easily functionalized by various materials/ chemicals, which renders it as an ideal surface modifier. In addition, PDA has absorption in NIR window and high photothermal conversion efficiency (40%), which makes it suitable as an efficient PA contrast agent (Lee et al., 2007). We further evaluated the potential of DCNP@PDA NP as a dual modal contrast agent for non-invasive visualization of GI tract and NIR-II imaging-guided intestinal obstruction surgery.

2. Experimental section

2.1. Materials and reagents

Dopamine hydrochloride was purchased from Alfa Aesar. Rare earth compounds of Yttrium (III) acetate hydrate ($(CH_3CO_2)_3Y \cdot xH_2O$, 99.9%), Ytterbium (III) acetate hydrate ($Yb(C_2H_3O_2)_3 \cdot xH_2O$, 99.9%), Erbium (III) acetate hydrate ($(CH_3CO_2)_3Er \cdot xH_2O$, 99.9%), Neodymium(III) acetate hydrate ($(CH_3CO_2)_3Nd \cdot xH_2O$, 99.9%), 1-Octadecene (ODE, 90%), oleic acid (OA, 90%), ammonia fluoride (NH_4F, 99.99% trace metals basis),

IGEPAL® CO-520 (($C_2H_4O)_n \cdot C_{15}H_{24}O$, ñ5), ammonium hydroxide solution (NH_4OH, 28%) and 3-(4, 5-dimethylthiazol-2-yl)-2, 5-diphenyltetrazolium bromide (MTT) were purchased from Sigma/ Aldrich. Dulbecco's modified Eagle's medium (DMEM) and fetal bovine serum (FBS) were obtained from Thermo Fisher Scientific. All materials were used without further purification. Milli-Q water (18.2 MΩ cm) was used in all experiments.

2.2. Instruments and characterizations

UV–Vis–NIR spectra were acquired by Agilent Cary 6000i UV/vis/ NIR spectrophotometer. The zeta potential was measured using zeta potentials analyzer (Malvern, Zetasizer Nano ZS90). The Fourier transform infrared (FTIR) spectra were recorded on a Bruker Vertex 70 spectrometer (Bruker, Germany). X-ray diffraction (XRD) patterns were obtained on a D8 ADVANCE X-ray diffractometer (Bruker, Germany). The transmission electron microscope (TEM) images were recorded with a FEI Tecnai G2 F20 X-TWIN transmission electron microscope operating at 120 kV. To obtain TEM images, samples were deposited and dried on copper grids covered with a carbon support film after glow discharged. The characterization of sizes of NPs by TEM was analyzed using ImageJ software. The results were obtained by counting a minimum of 100 particles in three discrete areas on TEM images. A designed and built system was used to acquire the NIR-II window fluorescence images (1000–1700 nm). The designed and built system for NIR-II *in vivo* and *in vitro* fluorescence imaging mainly includes a NIR vana InGaAs camera (Princeton Instruments, USA) with 640×512 focal plane array and 20 μm/pixel sensor, an integrated 808 nm laser diode system (fiber coupling laser system, 0–10 W, Changchun New Industries Optoelectronics Technology Co., Ltd.), and a customized imaging chamber. The excitation laser power was set to 4 W. The excitation light was filtered through a 1000 nm long-pass filter (Thorlabs, FEL1000) and focused onto the InGaAs detector by a 50 mm lens (f/1.4, Pentax). The images were acquired and analyzed by LightField software. The ImageJ software was used for image processing analysis and measurements. The PA signals were recorded using a Nexus 128 PA instrument (Endra Inc., Boston, MA) with a series of laser wavelengths in the range of 680–950 nm. The system is equipped with a tunable nanosecond pulsed laser (7 ns pulses, 20-Hz pulse repetition frequency, wavelength-dependent laser power density, about 4–7 mJ/pulse on the animal surface) and 128 unfocused ultrasound transducers (with 5 MHz center frequency and 3 mm diameter) arranged in a hemispherical bowl filled with water (temperature is set to 38 °C). The PA data is reconstructed in volumes of $256 \times 256 \times 256$ with $0.1 \times 0.1 \times 0.1$ mm voxels. The imaging data were analyzed using Osirix software (Pixmeo SARL, Bernex, Switzerland).

2.3. Synthesis of $NaYF_4$:Yb^{3+}, Er^{3+}@NaYbF @$NaYF_4$:Nd^{3+} DCNPs and DCNP@PDA NPs

The $NaYF_4$:Yb^{3+}, Er^{3+}@NaYbF @$NaYF_4$:Nd^{3+} DCNPs were prepared by a previously reported procedure (Shao et al., 2016). The DCNP@PDA NPs were synthesized according to our previously reported strategy (Liu et al., 2015; Ma et al., 2017). Typically, for synthesizing PDA-coated DCNP with 2 nm PDA shell, Igepal CO-520 (0.65 mL) was added in hexane (10 mL) containing oleic-acid-stabilized $NaYF_4$: Yb^{3+}, Er^{3+} @ $NaYbF_4$@$NaYF_4$:Nd^{3+} (10 mg). After stirred for 20 min, ammonium hydroxide (75 μL, 28 wt% in water) was added into mixture followed by ultrasonic treatment for 15 min. After stirred for another 30 min, dopamine hydrochloride aqueous solution (25 μL, 25 wt%) was

injected into the above reaction mixture at a rate of 3 μL min^{-1}. After stirred for 24 h, the NPs were precipitated by adding ethanol, collected by centrifugation (10 000 rpm for 10 min) and washed with ethanol and water (10 mL, three times). Finally, the UCNP@PDA NPs were dispersed in water and dried by vacuum evaporation.

2.4. Cell culture and cytotoxicity assay of DCNP@PDA NPs

The mouse embryonic fibroblast cell line NIH 3T3 cells were cultured with 100 μL of fresh culture medium (fresh DMEM supplemented with 10% FBS and 100 U/mL penicillin-streptomycin) in 96 well microtiter plate (8×10^3 cells per well) under a humidified 5% CO_2 at 37 °C for 24 h. After washed with 100 μL of fresh DMEM (3 times), fresh culture medium (100 μL) with various concentrations (100, 200, 400, 600, 800 and 1000 μg mL^{-1}) of DCNP@PDA NPs were added and incubated at same conditions for another 24 h, respectively. Subsequently, the cells were washed with 100 μL of PBS (3 times), and then 10 μL of MTT (5 mg/mL in PBS) and 100 μL of cell culturing solution were added into each well and incubated for another 4 h. Finally, the supernatant was discharged, and purple formazan product was dissolved by DMSO (100 μL per well) with gentle shaking to accelerate the dissolution of formazan and acquire the solution with uniform color for 10 min. The absorbance of each well was read on a Tecan Infinite M1000 Pro Microplate Reader at 510 nm and the medium oscillation frequency was chosen for shaking samples. The relative cell viabilities (%) were calculated by using the optical densities with respect to the control value. NIH 3T3 cells cultured without DCNP@PDA NPs were used as control samples.

2.5. Animal models

BALB/c nude mice (Charles River Laboratories, USA) were maintained in pathogen free conditions until imaging. All animal experiments were performed under the approval of Stanford University's Administrative Panel on Laboratory Animal Care.

2.6. NIR-II fluorescence imaging

The NIR-II fluorescence emission spectra were recorded under 808 nm continuous-wave (CW) laser excitation. The excitation laser power was set to 4 W. In order to reduce the background interference, the excitation light was filtered through a 1000 nm long-pass filter. For *in vitro* imaging, different concentrations of DCNP@PDA NP aqueous solution (100 μL per well) ranging from 20 nmol L^{-1} to 500 nmol L^{-1} were filled into 96-well plate (n = 3 per group). The exposure time was fixed at 200 ms. For *in vivo* imaging, 2% isoflurane in oxygen was used for anesthetizing the mice. A laser power density of 140 mW cm^{-2} was used to enable optimal temporal resolution. The exposure time varied from 100 to 1000 ms. For *ex vivo* imaging, the mice (n = 3 per group) were sacrificed at 7 days perfusion right after NIR-II FI and PAI. Organs including heart, liver, spleen, lungs, kidneys, stomach, duodenum, small intestine, large intestine, cecum, and rectum were dissected and collected. After being rinsed with PBS and drained with filter papers, the *ex vivo* images of organs were immediately acquired using the NIR-II fluorescence system with the same illumination setting as the *in vivo* imaging. The fluorescent images were processed with the same method as described previously.

2.7. Photoacoustic imaging

For *in vitro* imaging, different concentrations of DCNP@PDA NP aqueous solution ranging from 200 nmol L^{-1} to 800 nmol L^{-1} were filled into polyethylene capillaries (i.d. = 0.58 mm, o. d. = 0.965 mm, 3.0 m long, Becton Dickinson Co., MD). The ends of the fulfilled tube was rapidly sealed and then immersed in the water bath (38 °C) of the imaging tray to obtain the PA signals. For *in vivo* imaging, 2% isoflurane in oxygen was used for anesthetizing the mice (n = 3 per group). Then, the mice were placed at prone position in the imaging tray within the focal field of view (20 mm diameter sphere). The measurements of PA signals were quantitatively analyzed using Osirix software.

3. Results and discussion

3.1. Construction and characterization of DCNP@PDA NPs

As shown in Scheme 1, the construction of water-soluble $NaYF_4:Yb^{3+},Er^{3+}@NaYbF_4@NaYF_4:Nd^{3+}$ DCNP@PDA NPs involved two main steps: the synthesis of a hydrophobic oleic acid-capped DCNP and a hydrophilic DCNP@PDA NP *via* water-in-oil microemulsion method. The coating PDA shell can transfer the hydrophobic oleic acid capped DCNPs to aqueous solution due to its polar groups including hydroxyl and amine groups, endowing the DCNPs with improved hydrophilicity and stability.

The $NaYF_4:Yb^{3+},Er^{3+}@NaYbF_4@NaYF_4:Nd^{3+}$ DCNP was synthesized *via* a typical thermal deposition method (Shao et al., 2016). In the presence of ammonia water, the PDA shell grew on the surface of DCNP where the water droplets rendered a microreactor for the self-polymerization of dopamine under ambient condition (Liu et al., 2015; Ma et al., 2017). The morphologies of DCNPs and DCNP@PDA NPs were characterized by transmission electron microscope (TEM) and high-resolution transmission electron microscope (HRTEM). As shown in Fig. 1a, 1b and Fig. S1, the as-prepared DCNPs and DCNP@PDA NPs showed uniform sizes with the average diameters of 27.9 ± 1.8 nm and 32.3 ± 2.7 nm, respectively. A PDA outer shell with ~2 nm thickness was consistently and uniformly deposited on the DCNP surface without a significant multicore coating and core-free PDA NPs (as shown in Fig. 1d). X-ray diffraction (XRD) results indicated that the CSS DCNPs and DCNP@PDA NPs were of hexagonal crystallographic phase (JCPDS: 28–1192) with good crystallinity (as shown in Fig. 1e), which also confirmed by the HRTEM image (Fig. 1c). After the PDA shell coating, the XRD patterns of DCNP@PDA NPs were similar to DCNPs, indicating that the PDA coating cannot change the crystalline phase of DCNP. The Fourier transform infrared (FTIR) spectrum of as-prepared DCNP exhibited three IR bands at 1464 cm^{-1}, 2853 cm^{-1} and 2924 cm^{-1} (Fig. 1f), which were assigned to the –COOH stretching vibration, indicating that oleic acid molecules were attached on the DCNP surface during NPs synthesis. The DCNP@PDA NPs had three IR bands at 3380 cm^{-1} (NH stretching), 1585 cm^{-1} (C=C aromatic ring stretching vibration), and 1505 cm^{-1} (NH bending), which demonstrated the presence of PDA on DCNP.

As shown in Fig. S2, the zeta potential of DCNP@PDA NPs was 27.30 mV. Normally, neutrally and negatively charged NPs are less cytotoxic than positively charged ones, as they are less likely to be taken up *via* the negatively charged cell membrane (Schaeublin et al.,

2011). Because there were plenty of the substantive hydroxyl and amine groups on the DCNP@PDA NP surface, the DCNP@PDA NPs presented no detectable aggregation in complete medium including 10% fetal bovine serum (FBS) and high glucose Dulbecco modified Eagle medium (DMEM), and different pH values (1, 1.5, 2, 5.5, 6.5, 7.5, 8.5) of phosphate buffer solution (PBS) for as long as 7 days (Fig. S3), indicating that DCNP@PDA NPs had high colloidal stability. Furthermore, this was beneficial for the intended biomedical applications in the GI tract, which exhibits different pH values from acidic pH to basic pH (Evans et al., 1988).

3.2. Optical properties of DCNP@PDA NPs

We firstly investigated the absorption spectrum of DCNP@PDA NPs. The PA efficiency is strongly dependent on the photo-thermal conversion efficiency, which is affected by the absorption of the NPs. Assumed as a PAI probe, the NPs have to be excited in the tissue transparency window, for achieving deep and high resolution tissue imaging. The absorption spectrum of DCNP@PDA NPs exhibited broad band absorption in the NIR window (Fig. S4), which matched to the requirements for PAI probes. Under 808 nm CW laser excitation, DCNP@PDA NP exhibited three characteristic emission bands centered at 1000 nm for Yb^{3+}, 1060 nm and 1340 nm for Nd^{3+} (Fig. 2a), implying that it was suitable for FI in the NIR-II window. Due to the fluorescence quenching ability of PDA shell, the NIR-II fluorescence emission of DCNP@PDA NP was weaker than that of DCNP (shown in Fig. S5). As expected, the NIR-II fluorescence intensity of DCNP@PDA NPs showed excellent linearity with the concentrations of DCNP@PDA NPs in a range of 21–420 μg mL^{-1} ($R^2 =$ 0.986, as shown in Fig. 2b). After being corrected with the laser energy at different wavelengths, the PA spectra of DCNP@PDA NPs were obtained and shown as a function of wavelength in Fig. S6. The PA spectra exhibited a broad peak with the maximum PA intensity at 700 nm, extending over a wide NIR window (680–900 nm). Moreover, the PA intensities of DCNP@PDA NPs were linearly increased with increasing the mass concentrations of DCNP@PDA NPs in a range from 200 μg mL^{-1} to 800 μg mL^{-1} (as shown in Fig. 2c). Subsequently, the photostability of DCNP@PDA NPs was investigated under a long-term exposure of the laser radiation (Fig. 2d). Under irradiated by an 808 nm CW laser at a power density of 140 mW cm^{-2} for 1 h, the DCNP@PDA NPs exhibited less than 3% change of fluorescence intensity. Similarly, no PA amplitude was lost for DCNP@PDA NPs after exposure to a tunable nanosecond pulse laser. The results demonstrated that DCNP@PDA NPs had superior photostability and suitability for a long-term *in vivo* NIR-II FI and PAI.

3.3. In vivo visualization of GI tract with both NIR-II fluorescence and PA imaging

The Cytotoxicity of DCNP@PDA NPs was first investigated using NIH 3T3 cells (mouse embryonic fibroblast cells). After incubated with cells for 24 h, the DCNP@PDA NP showed a negligible cytotoxicity as high as the concentration of 1000 μg mL^{-1} (as shown in Fig. S7). The result demonstrated the DCNP@PDA NP had low cytotoxicity. Encouraged by the *in vitro* results, we investigated the potential of DCNP@PDA NP as an efficient NIR-II/PAI dual-modal nanoprobe through *in vivo* imaging the GI tract mice models, considering that diseases of GI tract are the most common problems in clinical practices.

The healthy BALB/c nude mice (n = 3) were treated by oral gavage with the DCNP@PDA NPs in PBS (0.15 mL, 800 μg mL^{-1}) for real-time imaging of intestinal motility and monitoring the behavior of the nanoprobe within the GI tract. NIR-II fluorescence images at different time points (2, 5, 10 min and 1, 3, 9, 24 h) of post-treatment were recorded under 808 nm CW laser irradiation with low power density (140 mW cm^{-2}, within the safety limits 329 mW cm^{-2} determined by the International Commission on Non-ionizing Radiation Protection) through an InGaAs camera (1000 ms exposure time) with a 1000 nm long-pass filter. As shown in Fig. 3a, the fluorescence signals were obtained in the stomach at 2 min post-gavage. As time moved on from 10 min to 9 h, the fluorescence signals were obtained in the duodenum, small intestine and large intestine. The fluorescence intensity movement in the small intestine indicated vigorous contractility with peristalsis and segmental contractions of the intestine at 1 h post-gavage. The NIR-II signal intensity in the small intestine was measured by plotting cross-sectional intensity profiles (marked by a white dash line, Fig. S8). Using the Gaussian-fitted full width at half maximum (FWHM) of the cross-sectional intensity profiles of the small intestine, we observed the FWHM was 2.59 mm and a higher signal-to-noise (S/N) ratio. No fluorescent signal of the abdomen was detected at 24 h post-gavage. These results illustrated that the DCNP@PDA NPs were largely excreted through the GI tract within 24 h and were not absorbed into the body through the intestine. The DCNP@PDA NPs used in GI tract imaging were excreted quickly due to low absorption in the GI tract while they would interact with serum plasma and the immune system by vein injection, leading to slow clearance routes of DCNP@PDA NPs through the hepatobiliary system.

In order to obtain the visualization of the lower abdomen clearly, the prepared DCNP@PDA NP probe was also perfused through anus. As shown in Fig. S9, the NIR-II fluorescence signals from large intestine, cecum and rectum could last 2 h. The prolonged time window exhibited particular valuable impact on the diagnosis of lower GI tract associated diseases. Therefore, the proposed high-performance DCNP@PDA NP has potential in the application of visualization of the GI tract in clinic.

Subsequently, DCNP@PDA NPs were used as PA contrast agent for PAI of GI tract *in vivo*. In this case, BALB/c nude mice (n = 3) were treated by oral gavage or anus perfused with the DCNP@PDA NPs (0.15 mL, 800 μg mL^{-1}), respectively. The cross-sectional PA signals of the stomach, duodenum, small intestine, large intestine, cecum and rectum were recorded at different time intervals of post-administration of the nanoprobe. As shown in Fig. 3b, DCNP@PDA NPs began to gradually fill the stomach and duodenum during the first 15 min post-gavage. DCNP@PDA NPs fully filled the small intestine at 105 min post-gavage, and deep tissue intestine imaging of live mice was achieved with high sensitivity. It is worth noting that negligible background is detected, which is enable to the clear discrimination of intestinal structure. More importantly, the arrangement and sequence of small intestinal loops were clearly observed (shown with white arrowheads), which facilitates the diagnosis of inflammatory, neoplastic intestinal lesions, and incidental extra-intestinal pathological changes. Clearly, compared with NIR-II FI, PA imaging possess microscopic imaging capability with spatial resolution, offering a complementary imaging modality to acquire comprehensive information (as shown in Fig. S8). The large intestine, cecum and rectum were fulfilled and clearly visualization through anus perfusion of the DCNP@PDA NPs (as

shown in Fig. S10). Furthermore, DCNP@PDA NPs perfused through anus were mostly drained from the GI tract in 24 h, which could decrease the possibility of further toxicity to many normal organs. Following the progression of the NPs in the GI tract, DCNP@PDA NPs gradually journeyed from the stomach, small intestine, through the large intestine, cecum, rectum and finally, were expelled by defecation. The results of *in vivo* NIR-II FI and PAI demonstrated that the as-prepared DCNP@PDA NP could potentially serve as a dual-modal NIR-II/PAI probe for functional GI tract imaging.

3.4. Diagnosis of GI peristalsis disorder and NIR-II imaging-guided intestinal obstruction surgery

A mouse model of intestinal partial obstruction was built according to the reported methods for investigating the ability of the DCNP@PDA NPs to diagnose intestinal diseases such as obstructions which impede or block peristaltic movement (Ha et al., 2018). Partial obstruction was surgically induced in BALB/c nude mice (n = 3) by placing a silicone ring around the junction of duodenum and small intestine. This ring created a partial blockage in the small intestine. Then, DCNP@PDA NPs (0.15 mL, 800 μg mL^{-1}) were given to the mice with intestinal obstruction through oral gavage. The NIR-II fluorescence images were recorded at different time intervals of post-gavage. As shown in Fig. 4a, the stomach and duodenum were partially filled and distended from 1 min to 50 min at post-gavage. However, the phenomenon exhibited differences in the intestinal distribution of the DCNP@PDA NPs between the mice with obstruction and healthy mice. At 50 min post-gavage, the junction of duodenum and small intestine showed strong NIR-II fluorescence signal, indicating that the DCNP@PDA NPs were accumulated in these parts. The observation suggested that DCNP@PDA NPs were suitable for diagnosis of GI peristalsis disorder.

With the help of the NIR-II FI set up and the outstanding optical property of DCNP@PDA NPs, the potential application for image-guided intestinal obstruction mapping and surgery was evaluated. The mice with intestinal obstruction were treated by DCNP@PDA NPs through oral gavage. As shown in Fig. 4b, intestinal obstruction position was notably identified at 10 min post-gavage. The intestinal obstruction became visible and distinguishable, and exhibited increased fluorescent signal over time. Under NIR-II FI guidance, the obstruction was precisely dissected in a short time, mimicking the standard procedure as in clinical obstruction surgery. The whole surgery process was demonstrated by the recorded Movie S1. To verify the intestinal obstruction was removed successfully, the NIR-II FI of GI tract was carried out. As shown in Fig. 4c, DCNP@PDA NPs passed through the obstructive site and discharged successfully after 24 h post-gavage, which were consistent with the intestinal distribution of healthy mice. The intestinal obstruction can be successfully removed under NIR-II bioimaging guidance, suggesting potential precise clinical application of the DCNP@PDA NPs as efficient NIR-II FI nanoprobes.

3.5. Histological analysis and biodistribution

It is extremely essential to possess the high biocompatibility and low biotoxicity of NPs for biomedical applications. The *in vivo* toxicity evaluation of DCNP@PDA NPs was performed by a typical histological assessment method. Fig. 5 shows the histological

analysis of H&E stained organs (heart, liver, spleen, lung, kidney, stomach, duodenum, small intestine, large intestine, cecum and rectum) of BLAC/c nude mice perfused with DCNP@PDA NPs orally at 7 days. The normally raised mice were used as a control group. No apparent lesions in the isolated organs were observed. To understand the biodistribution and clearance of DCNP@PDA NPs in the mice, the *ex vivo* NIR-II fluorescence images of the major organs and the concentrations of Yb (the elemental constituents of DCNP@PDA NPs) in vital organs were investigated. As shown in Fig. S11 and Fig. S12, the biodistribution of DCNP@PDA NPs in various organs showed no obvious differences between the treated mice and control mice. It further confirmed that DCNP@PDA NPs were well intact in the GI of the mice for a certain period before excretion and did not enter in circulatory system via the absorption of small intestine. These results indicated the DCNP@PDA NPs had no observable *in vivo* toxicity.

3.6. Discussion

In this study, we have successfully demonstrated the feasibility of using a melanin-coated lanthanide doped DCNP to perform dual NIR-II FI and PAI *in vitro* and *in vivo*. Both NIR-II FI and PAI modalities retain their own unique strengths in terms of sensitivity, spatial resolution, temporal resolution, and depth of tissue penetration for noninvasive imaging. The combination of the two modalities has the prominent effect of synergistic enhancement, which could improve the accuracy in diagnosis and the acquisition of complementary molecular information at targeted sites.

The main motivation of this study is to obtain multiform-dimension information from different perspectives by combining NIR-II FI and PAI modalities in one imaging agent. Herein, we fabricated DCNP as an efficient NIR-II imaging probe. Compared to the reported kinds of NIR-II fluorophores, the DCNP has the advantages of low photobleaching, long luminescence lifetimes, low long-term cytotoxicity and narrow emission band widths. When the DCNP is coated with melanin-inspired PDA polymer to form water-soluble NPs, the DCNP@PDA NP not only exhibits strong fluorescence in the NIR-II window, PDA shell can also be used as an efficient PA contrast agent. Especially, the DCNP@PDA has good stability even in harsh GI environments after oral administration. The superior properties of DCNP@PDA NP guarantee the fluorescence/ PA imaging acquisition with high contrast, significantly reducing minimal interference between NIR-II fluorescence and PA effect when the same contrast agent is used simultaneously for both NIR-II FI and PAI.

In addition, it is of great importance to optimize the suitable mixture ratio in order to reduce the interferences between two imaging modalities. Accompanies with the reduction in the dosages, side effects can be minimized as well. It is worthy of noting that the strong absorbance of PDA generally quenches the emission of fluorophores. It's thus important to optimize the suitable mixture ratio between DCNPs and PDA shell. As shown in Fig. 2 and Fig. S5, the PA signal is proportional to the concentration which is attributed to the content of PDA, while the NIR-II fluorescence emission of DCNP is reduced *ca.* 2.5 times after coated by PDA due to the strong absorbance of PDA. But, DCNP@PDA NPs still emit strong NIR-II fluorescence enough for clearly visualization of GI tract. Moreover, in order to use one single dose of DCNP@PDA NPs obtaining high sensitivities of both NIR-II FI and

PAI, a PDA outer shell with ~2 nm thickness has been selected for further use. A single dose of DCNP@PDA NPs leads to high sensitivities of both NIR-II FI and PAI, indicating it sufficiently meets the urgent need to develop multimodal contrast agents requiring only one dose.

Finally, the use of dual NIR-II FI and PAI is of great importance in precision medicine research. Herein, we combine both NIR-II FI and PAI modalities for GI tract, since it is still difficult to get an accurate and conclusive description of GI tract associate disease status (especially small intestine) due to the length, complex loops, and peristalsis. Generally speaking, visual examinations of the anatomy and pathology of the GI tract are the routine and essential means in diagnosis of GI diseases to ensure that patients can receive less invasive treatments and have a good quality of life (Zheng et al., 2015). GI tract imaging is a widely used clinical method for diagnosis of structural diseases in digestive system. However, traditional GI tract imaging is affected by its inherent defects, such as poor spatiotemporal resolution, risk of contrast agent allergy, and exposure to X-ray radiation, which limit its applications in clinical medicine. Therefore, there is a great demand for the development of safe and effective imaging methods in clinical diagnosis of GI diseases (Zebibula et al., 2018). NIR-II fluorescence imaging may provide a reliable method for monitoring intestinal motility disorders or dysfunction and providing evaluation information of GI therapeutic agents *in vivo* due to its superior spatiotemporal resolution (Lin et al., 2019). Recently, bioimaging in the NIR-II window has been successfully applied for real-time GI tract and image-guided surgery (Lin et al., 2019; Wang et al., 2018). Inspired by the crucial status of fault-free diagnosis of GI diseases, PAI is greatly welcomed to achieve precise synergistic imaging outcomes. In addition, PAI is a safe, non-invasive and non-ionizing modality, which matches the preferred characteristics of GI imaging, especially in the case of pediatric patients (Zhang et al., 2014). Thus, as a proof-of-concept experiment, we demonstrated the feasibility of DCNP@PDA NP for *in vivo* NIR-II/PA dual-modal imaging of GI tract with high penetration depth and remarkable temporal-spatial resolution. NIR-II FI modality provides the real-time visualization of the whole trail of DCNP@PDA NP probes within the GI tract, while PAI modality provides the detailed information with high quality spatial resolution and deep tissue penetration (such as the loop structure of small intestine) in small animal models. Moreover, *in vivo* imaging of animal models of human diseases serves as a pivotal translational link between fundamental research and clinical applications. Through our experiments, the dual NIR-II FI and PAI nanoprobe has a potential to a precise diagnosis of GI diseases, especially coupled with endoscopy techniques.

4. Conclusions

In summary, high quality DCNP@PDA NPs with uniform size, excellent monodispersity, good biocompatibility, favorable chemical stability in harsh environments of GI system, and ultrahigh efficiency of NIR-II fluorescence and PA imaging have been explored. The nanoprobe can be used for broad biomedical applications including as a novel NIR-II FI/PAI probe for GI tract visualization, diagnosis of GI peristalsis disorder and NIR-II FI-guided intestinal obstruction surgery.

Supplementary Material

Refer to Web version on PubMed Central for supplementary material.

Acknowledgment

References

Ai T, Shang W, Yan H, Zeng C, Wang K, Gao Y, Guan T, Fang C, Tian J, 2018. Biomaterials 167, 216–225. [PubMed: 29573651]

Antaris AL, Chen H, Cheng K, Sun Y, Hong G, Qu C, Diao S, Deng Z, Hu X, Zhang B, Zhang X, Yaghi OK, Alamparambil ZR, Hong X, Cheng Z, Dai H, 2016. Nat. Mater 15 (2), 235–242. [PubMed: 26595119]

Antaris AL, Chen H, Diao S, Ma Z, Zhang Z, Zhu S, Wang J, Lozano AX, Fan Q, Chew L, Zhu M, Cheng K, Hong X, Dai H, Cheng Z, 2017. Nat. Commun 8, 15269. [PubMed: 28524850]

Antaris AL, Robinson JT, Yaghi OK, Hong G, Diao S, Luong R, Dai H, 2013. ACS Nano 7 (4), 3644–3652. [PubMed: 23521224]

Chen G, Ohulchanskyy TY, Liu S, Law W-C, Wu F, Swihart MT, Agren H, Prasad PN, 2012. ACS Nano 6 (4), 2969–2977. [PubMed: 22401578]

Chen G, Qju H, Prasad PN, Chen X, 2014. Chem. Rev 114 (10), 5161–5214. [PubMed: 24605868]

Cheng K, Chen H, Jenkins CH, Zhang G, Zhao W, Zhang Z, Han F, Fung J, Yang M, Jiang Y, Xing L, Cheng Z, 2017. ACS Nano 11 (12), 12276–12291. [PubMed: 29202225]

Choi J-S, Kim S, Yoo D, Shin T-H, Kim H, Gomes MD, Kim SH, Pines A, Cheon J, 2017. Nat. Mater 16 (5), 537–542. [PubMed: 28166216]

Dai Y, Yang D, Yu D, Cao C, Wang Q, Xie S, Shen L, Feng W, Li F, 2017. ACS Appl. Mater. Interfaces 9 (32), 26674–26683. [PubMed: 28726368]

Evans DF, Pye G, Bramley R, Clark AG, Dyson TJ, Hardcastle JD, 1988. Gut 29 (8), 1035–1041. [PubMed: 3410329]

Fan Y, Wang P, Lu Y, Wang R, Zhou L, Zheng X, Li X, Piper JA, Zhang F, 2018. Nat. Nanotechnol 13 (10), 941–946. [PubMed: 30082923]

Fan Y, Zhang F, 2019. Adv. Opt. Mater 1801417.

Gibbs SL, 2012. Quant. Imaging Med. Surg 2 (3), 177–187. [PubMed: 23256079]

Guo B, Feng Z, Hu D, Xu S, Middha E, Pan Y, Liu C, Zheng H, Qian J, Sheng Z, Liu B, 2019. Adv. Mater 31, 1902504.

Ha SE, Wei L, Jorgensen BG, Lee MY, Park PJ, Poudrier SM, Ro S, 2018. J. Vis. Exp 133, e57381.

He S, Song J, Liu J, Liu L, Qu J, Cheng Z, 2019. Adv. Opt. Mater 7, 1900045.

Hong G, Antaris AL, Dai H, 2017. Nat. Biomed. Eng 1, 0010.

Hong G, Robinson JT, Zhang Y, Diao S, Antaris AL, Wang Q, Dai H, 2012. Angew. Chem. Int. Ed 51 (39), 9818–9821.

Hong G, Zou Y, Antaris AL, Diao S, Wu D, Cheng K, Zhang X, Chen C, Liu B, He Y, Wu JZ, Yuan J, Zhang B, Tao Z, Fukunaga C, Dai H, 2014. Nat. Commun 5, 4206. [PubMed: 24947309]

Hu X, Tang Y, Hu Y, Lu F, Lu X, Wang Y, Li J, Li Y, Ji Y, Wang W, Ye D, Fan Q, Huang W, 2019. Theranostics 9 (14), 4168–4181. [PubMed: 31281539]

Jiang Y, Pu K, 2017. Small 13 (30), 1700710.

Keereweer S, Van Driel PBAA, Snoeks TJA, Kerrebijn JDF, de Jong RJB, Vahrmeijer AL, Sterenborg HJCM, Lowik CWGM, 2013. Clin. Cancer Res 19 (14), 3745–3754. [PubMed: 23674494]

Kim H, Beack S, Han S, Shin M, Lee T, Park Y, Kim KS, Yetisen AK, Yun SH, Kwon W, Hahn SK, 2018. Adv. Mater 30 (10), 1701460.

Kircher MF, de la Zerda A, Jokerst JV, Zavaleta CL, Kempen PJ, Mittra E, Pitter K, Huang R, Campos C, Habte F, Sinclair R, Brennan CW, Mellinghoff IK, Holland EC, Gambhir SS, 2012. Nat. Med 18 (5), 829–834. [PubMed: 22504484]

Lee H, Dellatore SM, Miller WM, Messersmith PB, 2007. Science 318 (5849), 426–430. [PubMed: 17947576]

Li B, Lu L, Zhao M, Lei Z, Zhang F, 2018. Angew. Chem. Int. Ed 57 (25), 7483–7487.

Lin J, Zeng X, Xiao Y, Tang L, Nong J, Liu Y, Zhou H, Ding B, Xu F, Tong H, Deng Z, Hong X, 2019. Chem. Sci 10 (4), 1219–1226. [PubMed: 30774922]

Liu F, He X, Lei Z, Liu L, Zhang J, You H, Zhang H, Wang Z, 2015. Adv. Healthc. Mater 4 (4), 559–568. [PubMed: 25471617]

Liu L, Wang S, Zhao B, Pei P, Fan Y, Li X, Zhang F, 2018. Angew. Chem. Int. Ed 57 (25), 7518–7522.

Liu Y, Ai K, Liu J, Deng M, He Y, Lu L, 2013. Adv. Mater 25 (9), 1353–1359. [PubMed: 23280690]

Liu Y, Ai K, Lu L, 2014. Chem. Rev 114 (9), 5057–5115. [PubMed: 24517847]

Ma L, Liu F, Lei Z, Wang Z, 2017. Biosens. Bioelectron 87, 638–645. [PubMed: 27619527]

Nguyen QT, Tsien RY, 2013. Nat. Rev. Cancer 13 (9), 653–662. [PubMed: 23924645]

Qin C, Cheng K, Chen K, Hu X, Liu Y, Lan X, Zhang Y, Liu H, Xu Y, Bu L, Su X, Zhu X, Meng S, Cheng Z, 2013. Sci. Rep 3, 1490. [PubMed: 23508226]

Schaeublin NM, Braydich-Stolle LK, Schrand AM, Miller JM, Hutchison J, Schlager JJ, Hussain SM, 2011. Nanoscale 3 (2), 410–420. [PubMed: 21229159]

Shao W, Chen G, Kuzmin A, Kutscher HL, Pliss A, Ohulchanskyy TY, Prasad PN, 2016. J. Am. Chem. Soc 138 (50), 16192–16195. [PubMed: 27935695]

Sheng Z, Guo B, Hu D, Xu S, Wu W, Liew WH, Yao K, Jiang J, Liu C, Zheng H, Liu B, 2018. Adv. Mater 30, 1800766.

Shou K, Qu C, Sun Y, Chen H, Chen S, Zhang L, Xu H, Hong X, Yu A, Cheng Z, 2017. Adv. Funct. Mater 27 (23), 1700995. [PubMed: 29623009]

Vahrmeijer AL, Hutteman M, van der Vorst JR, van de Velde CJH, Frangioni JV, 2013. Nat. Rev. Clin. Oncol 10 (9), 507–518. [PubMed: 23881033]

Wang LV, Hu S, 2012. Science 335 (6075), 1458–1462. [PubMed: 22442475]

Wang P, Fan Y, Lu L, Liu L, Fan L, Zhao M, Xie Y, Xu C, Zhang F, 2018. Nat. Commun 9, 2898. [PubMed: 30042434]

Wang Q, Dai Y, Xu J, Cai J, Niu X, Zhang L, Chen R, Shen Q, Huang W, Fan Q, 2019. Adv. Funct. Mater 1901480.

Wong MH, Giraldo JP, Kwak S-Y, Koman VB, Sinclair R, Lew TTS, Bisker G, Liu P, Strano MS, 2017. Nat. Mater 16 (2), 264–272. [PubMed: 27798623]

Xie X, Gao N, Deng R, Sun Q, Xu Q-H, Liu X, 2013. J. Am. Chem. Soc 135 (34), 12608–12611. [PubMed: 23947580]

Xu J, Gulzar A, Yang P, Bi H, Yang D, Gai S, He F, Lin J, Xing B, Jin D, 2019. Coord. Chem. Rev 381, 104–134.

Yang T, Tang Y, Liu L, Lv X, Wang Q, Ke H, Deng Y, Yang H, Yang X, Liu G, Zhao Y, Chen H, 2017. ACS Nano 11, 1848–1857. [PubMed: 28117993]

Yi H, Ghosh D, Ham M-H, Qi J, Barone PW, Strano MS, Belcher AM, 2012. Nano Lett. 12 (3), 1176–1183. [PubMed: 22268625]

Zebibula A, Alifu N, Xia L, Sun C, Yu X, Xue D, Liu L, Li G, Qian J, 2018. Adv. Funct. Mater 28 (9), 1703451.

Zhang M, Yue J, Cui R, Ma Z, Wan H, Wang F, Zhu S, Zhou Y, Kuang Y, Zhong Y, Pang D-W, Dai H, 2018. Proc. Natl. Acad. Sci. U.S.A 115 (26), 6590–6595. [PubMed: 29891702]

Zhang R, Xu Y, Zhang Y, Kim HS, Sharma A, Gao J, Yang G, Kim JS, Sun Y, 2019. Chem. Sci 10, 8348–8353. [PubMed: 31803412]

Zhang Y, Hong G, Zhang Y, Chen G, Li F, Dai H, Wang Q, 2012. ACS Nano 6 (5), 3695–3702. [PubMed: 22515909]

Zhang Y, Jeon M, Rich LJ, Hong H, Geng J, Zhang Y, Shi S, Barnhart TE, Alexandridis P, Huizinga JD, Seshadri M, Cai W, Kim C, Lovell JF, 2014. Nat. Nanotechnol 9 (8), 631–638. [PubMed: 24997526]

Zheng X, Shi J, Bu Y, Tian G, Zhang X, Yin W, Gao B, Yang Z, Hu Z, Liu X, Yan L, Gu Z, Zhao Y, 2015. Nanoscale 7 (29), 12581–12591. [PubMed: 26145146]

Zhong Y, Ma Z, Zhu S, Yue J, Zhang M, Antaris AL, Yuan J, Cui R, Wan H, Zhou Y, Wang W, Huang NF, Luo J, Hu Z, Dai H, 2017. Nat. Commun 8, 737. [PubMed: 28963467]
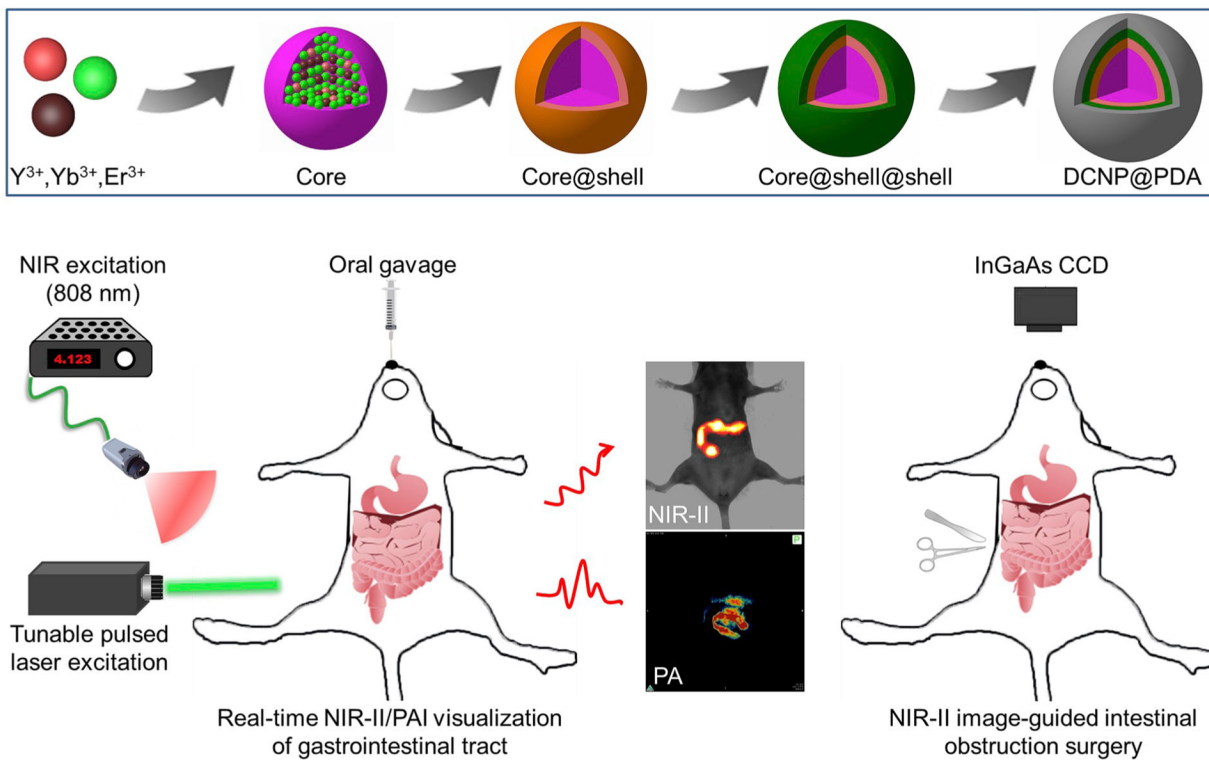
Scheme 1.
Illustration of the DCNP@PDA NP fabrication for dual-modal NIR-II/PAI visualization of GI tract *in vivo* and NIR-II image-guided intestinal obstruction surgery. Core, core@shell and core@shell@shell represent $NaYF_4:Yb^{3+},Er^{3+}$, $@NaYF_4:Yb^{3+},Er^3$ $@NaYbF_4$, and $NaYF_4:Yb^{3+},Er^{3+}$ $@NaYbF_4@NaYF_4:Nd^{3+}$, respectively.
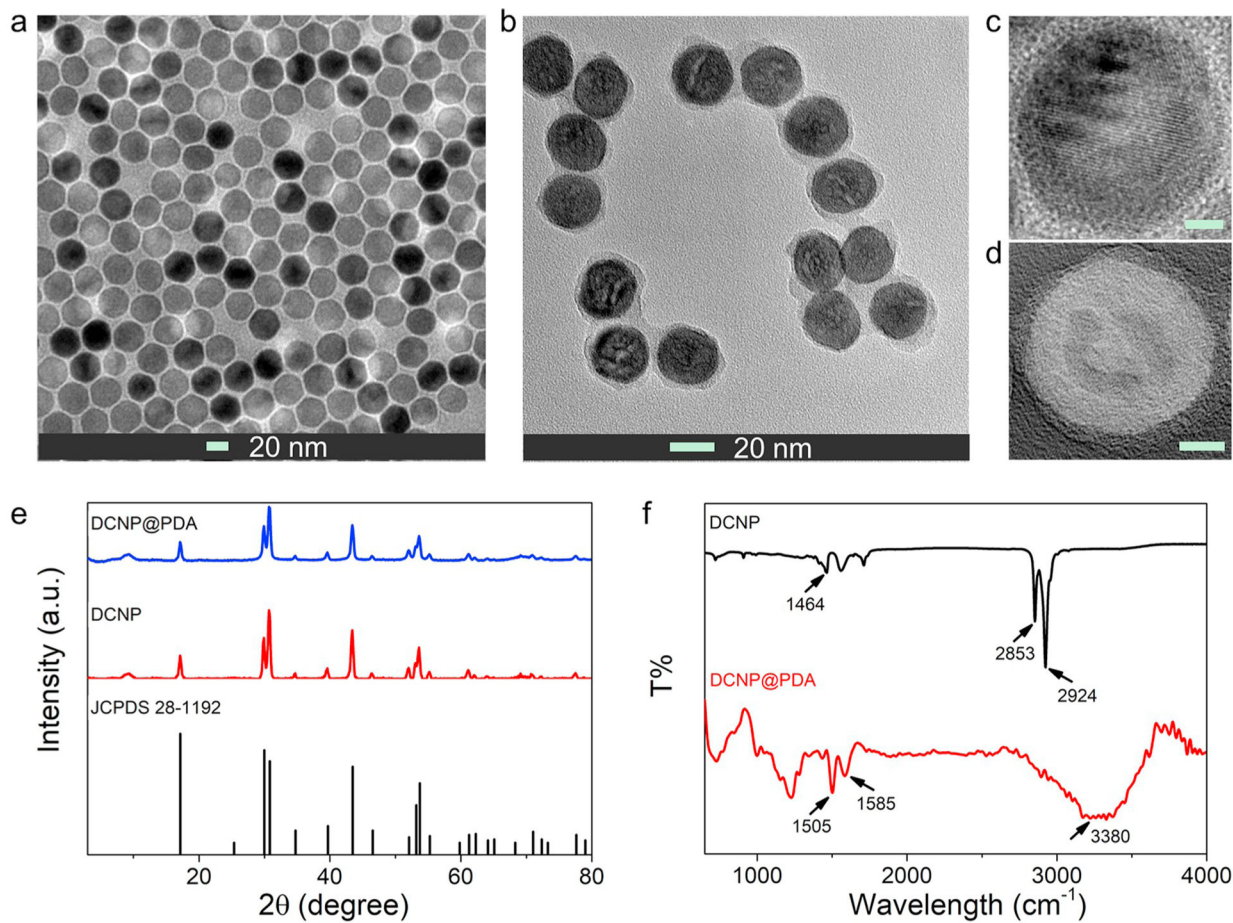
Fig. 1.
TEM images of (a) $NaYF_4$:Yb^{3+},Er^{3+}@$NaYbF_4$@$NaYF_4$:Nd^{3+} core@shell@shell DCNPs and (b) DCNP@PDA NPs. The corresponding HRTEM images of (c) DCNPs and (d) DCNP@PDA NPs, respectively. The scale bars are 5 nm. (e) XRD patterns of DCNPs and DCNP@PDA NPs, respectively. (f) FTIR spectra of DCNPs and DCNP@PDA NPs, respectively.
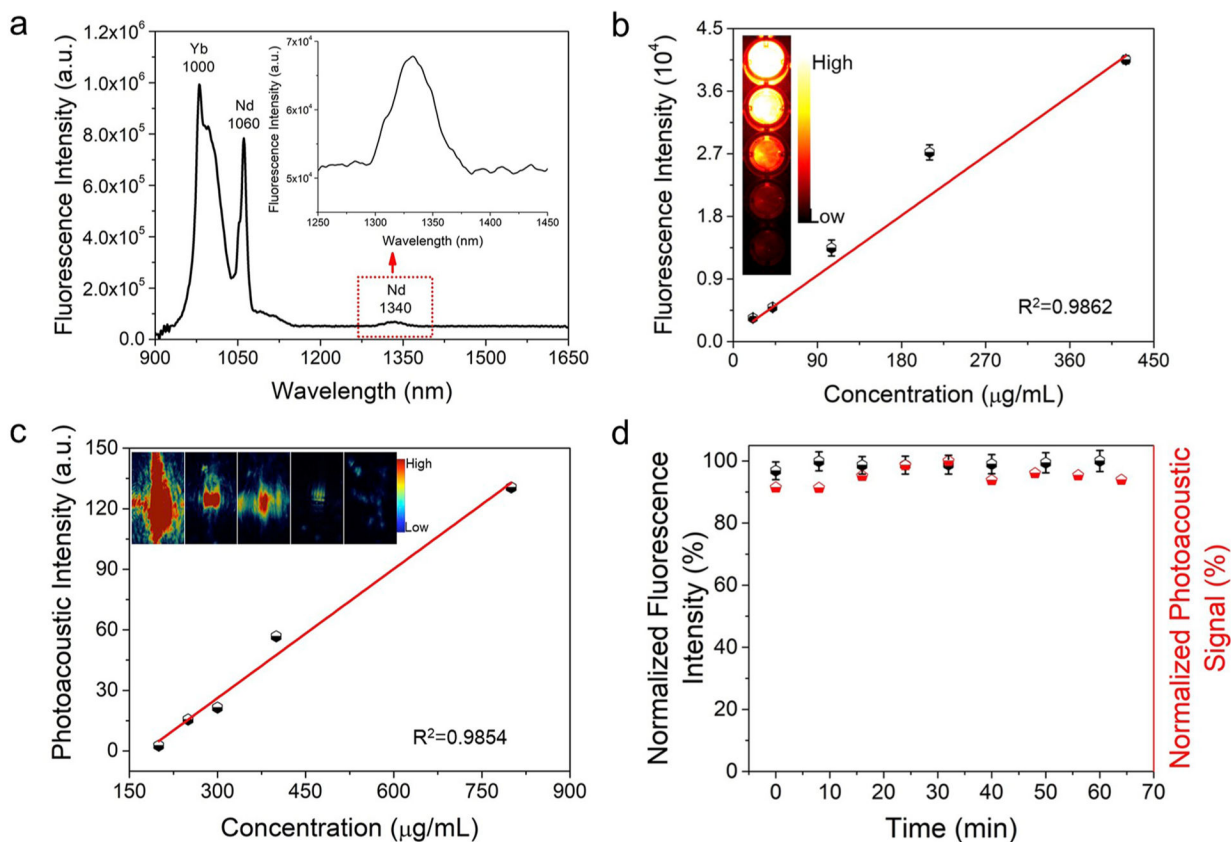
Fig. 2.
Optical properties of DCNP@PDA NPs. (a) NIR-II emission spectrum of DCNP@PDA NPs under 808 nm CW laser excitation. (b) The NIR-II fluorescence intensities of DCNP@PDA NPs as a function of mass concentrations of the DCNP@PDA NPs under 808 nm CW laser excitation, with a 1000 nm long-pass filter. (c) The PA amplitudes of DCNP@PDA NPs at 700 nm as a function of mass concentrations of DCNP@PDA NPs. (d) Photostability of DCNP@PDA NPs in terms of normalized fluorescence intensities (black symbols) and PA amplitudes (red symbols) under a 808 nm CW laser exposure and a 700 nm pulse laser irradiation for 1 h, respectively.
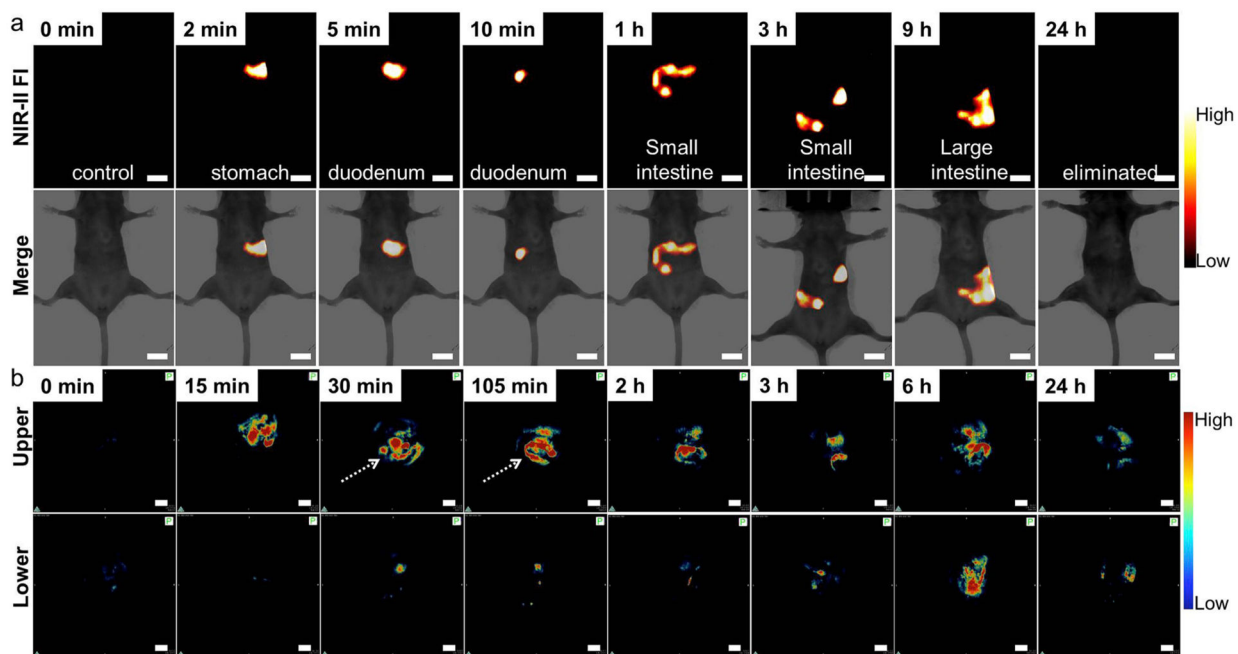
Fig. 3.
(a) *In vivo* NIR-II FI for GI tract of the BALB/c nude mouse at different time intervals after oral gavage of DCNP@PDA NPs under 808 nm CW laser irradiation and 1000 ms imaging exposure time. (b) *In vivo* PAI for GI tract of upper section and corresponding lower section of the BALB/c nude mouse at different time intervals after oral gavage of DCNP@PDA NPs. Scale bars are 10 mm.
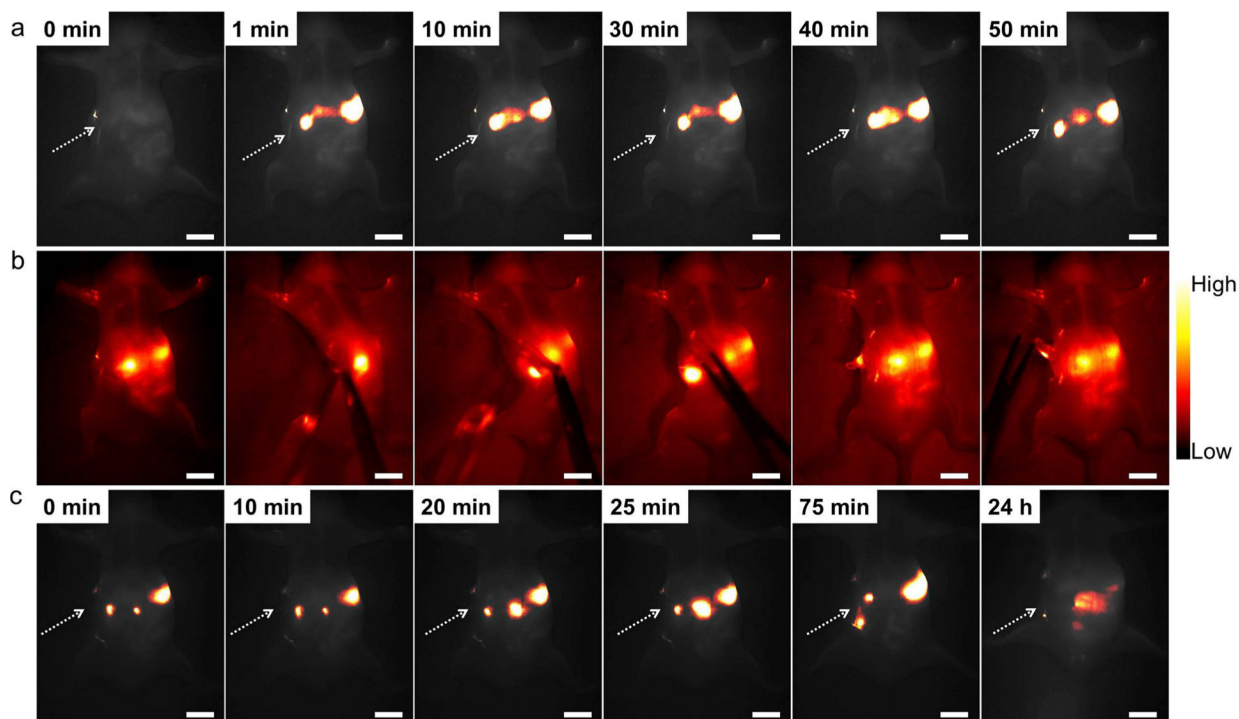
Fig. 4.
(a) Representative *in vivo* NIR-II fluorescence images of a BALB/c nude mouse with intestinal obstruction. Compared with GI tract images, DCNP@PDA NPs still accumulated at the obstructive sites even at 50 min post-gavage. (b) *In vivo* NIR-II FI-guided intestinal obstruction mapping on BALB/c nude mice. (c) *In vivo* NIR-II FI of GI tract after intestinal obstruction surgery. DCNP@PDA NPs passed through the obstructive site and discharged successfully after 24 h post-gavage. Scale bars are 10 mm.
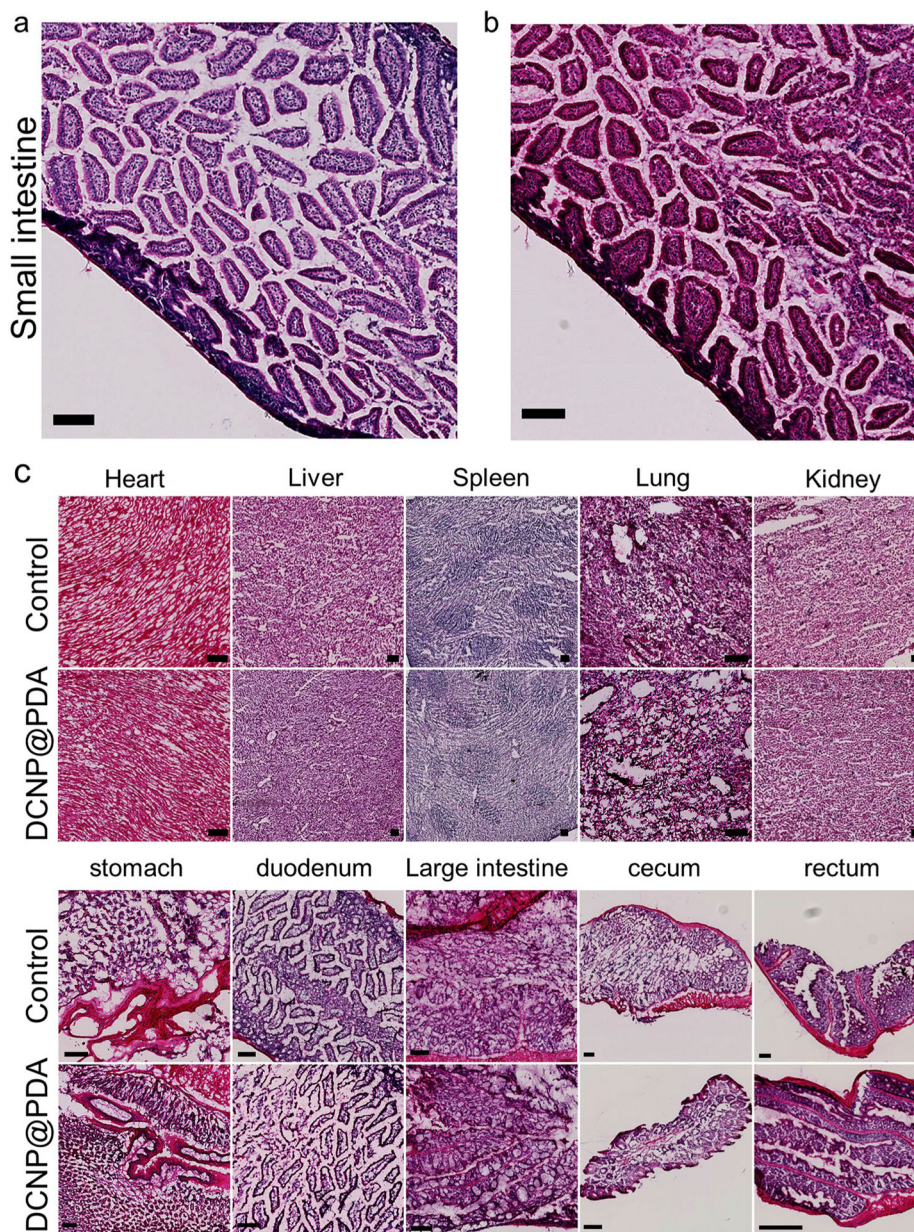
Fig. 5.
Representative H&E stained images of (a) vital organ small intestine section of BALB/c nude mice untreated and (b) after oral gavage with DCNP@PDA NPs at 7 days, respectively, and (c) major organs including heart, liver, spleen, lung, kidney, stomach, duodenum, large intestine, cecum and rectum collected from the untreated mice (Control) and $NaYF_4:Yb^{3+},Er^{3+}@NaYbF_4@NaYF_4:Nd^{3+}$ @PDA NPs perfused mice at 7 days. No obvious organ damage or lesion was observed for $NaYF_4:Yb^{3+},Er^{3+}@NaYbF_4@NaYF_4:Nd^{3+}$ @PDA NPs treated mice. Scale bar: 100 μm.